REPORT NO.
UCB/SEMM-95/13

STRUCTURAL ENGINEERING
MECHANICS AND MATERIALS

RECENT DEVELOPMENTS IN THE FORMULATION OF ASSUMED ENHANCED STRAIN FINITE ELEMENTS FOR FINITE DEFORMATION PROBLEMS

BY

S. GLASER
AND
F. ARMERO

DECEMBER 1995

DEPARTMENT OF CIVIL ENGINEERING
UNIVERSITY OF CALIFORNIA
BERKELEY, CALIFORNIA

Recent Developments in the Formulation of Assumed Enhanced Strain Finite Elements for Finite Deformation Problems

by

S. GLASER & F. ARMERO

Structural Engineering, Mechanics and Materials
Department of Civil Engineering
University of California, Berkeley, CA 94720

Abstract

This paper presents recent advances obtained by the authors in the development of enhanced strain finite elements for finite deformation problems. Two options are discussed, both involving simple modifications of the original enhancement strategy of the deformation gradient as proposed in SIMO & ARMERO [1992] and SIMO, ARMERO & TAYLOR [1993]. The first new strategy is based on a full symmetrization of the original enhanced interpolation fields. The second family of elements involves only the transpose part of the enhanced interpolation fields. The new elements are formulated in plane strain, axisymmetric and full three dimensional conditions. Both simple modifications lead to a significant improvement of the performance in problems involving high compressive stresses, showing in particular a mode-free response, while maintaining a simple and efficient (strain driven) numerical implementation. These properties are demonstrated with a number of numerical benchmark simulations.

1. Introduction

The formulation of low order finite elements in the finite deformation range that exhibit improved properties over the basic Galerkin approach is of the maximum interest. For instance, the locking-free response in the incompressible limit and in bending dominated problems, together with a good accuracy for coarse meshes, are some of the properties required for typical practical applications. A good response in localization problems is also a desired feature in problems involving large inelastic strains. These properties have to be combined with a simple numerical implementation, even in the general context of elasto-plastic and fully coupled materials models, thus leading almost inevitably to formulations based on a strain driven structure. The effectiveness observed by low order elements in this general class of problems, especially in problems involving contact, has led to an intensive research in this area.

Recently, SIMO & ARMERO [1992] presented the formulation of bilinear and trilinear finite elements for two and three dimensional finite deformation problems, respectively, that exhibit these properties. The proposed approach is an extension to the geometrically

nonlinear range of the enhanced strain formulation originally proposed in SIMO & RIFAI [1991] for infinitesimal problems, inspired to a large extent by the excellent performance of the now classical QM6 element proposed originally in TAYLOR et al [1976]. The proposed formulation consisted in a local additive enhancement of the deformation gradient, leading altogether to a very simple and efficient numerical implementation. However, the elements developed in this framework (denoted by Q1/E4, Q1/E5, and Q1/E9 for plane strain, axisymmetric, and three dimensional problems, respectively) show hourglass modes for large strains, especially in compression, as reported in SIMO & ARMERO [1993]. An improvement of the original formulation has been presented in SIMO, ARMERO & TAYLOR [1993]. A completely locking-free element in 3D, referred to as QM1/E12, was proposed in combination with an improved quadrature rule. Even though initial numerical tests showed a significant improvement with the modified integration rule even in the plane strain case, the hourglass modes persisted as more recent analyses have shown. In this respect, the analysis presented in WRIGGERS & REESE [1994] identified the appearance of a (non-physical) zero eigenvalue at a certain deformation of the compression of a single quadrilateral element. The problem that these authors considered, involving an homogeneous state of strain of a hyperelastic material, allowed the analytical characterization of this mode. Several authors (SOUZA et al [1995], CRISFIELD et al [1995] among others) have reported similar performances posteriorly.

Given these difficulties, several authors have proposed alternative elements based on different enhancement strategies. For instance, NAGTEGAAL & FOX [1995] describe the incremental enhancement of the deformation gradient implemented recently in ABAQUS, whereas CRISFIELD et al [1995] propose the enhancement of the right stretch tensor as an alternative. While the former appears to exhibit the same drawbacks as the original formulation, the latter approach appears to lead to an improved performance at the cost of a rather difficult and intricate numerical implementation. In this paper, we propose a simple modification of the original formulation presented in SIMO & ARMERO [1992] that leads to a mode-free element for the compression test problems considered so far, while maintaining a simple numerical implementation. As described in detail below, the modification proposed herein involves simple modifications of the enhanced interpolations fields presented originally in this last reference.

However, despite these improved properties in compression, hourglass modes have been observed at large tensile strains in inelastic models. These modes are also exhibited by the original enhanced formulation in SIMO & ARMERO [1992], SIMO, ARMERO & TAYLOR [1993] as well as by the aforementioned alternative approaches in NAGTEGAAL et al [1995] and CRISFIELD et al [1995]. The origin of these difficulties has been traced to the appearance of a (physical) negative axial stiffness, which is transmitted to the bending modes, leading to a classical hourglass pattern. negative stiffness is associated to the stretching mode. Even though the origin of these modes has been fully characterized, further research is required for the formulation of elements that avoid this problem. An

possible alternative involving an hourglass control parameter is proposed herein.

An outline of the rest of the paper is as follows. Section 2 describes the enhancement of the deformation gradient for the proposed elements. Section 3 includes the derivation of the (weak) finite element equations. The finite element equations, including their linearization, are described in detail for the model problem of finite deformation hyperelasticity. Section 4 includes a number of representative numerical simulations that assess the performance of these elements in elastic and inelastic simulations. Both two and three dimensional problems are considered. Finally, conclusions are drawn in Section 5.

2. The Assumed Enhanced Deformation Gradient

Denote by Ω^h a discretization in quadrilateral finite elements if $n_{\text{dim}} = 2$ or brick elements if $n_{\text{dim}} = 3$ of the domain $\Omega \subset \mathbb{R}^{n_{\text{dim}}}$ occupied by the reference placement of a solid $\mathcal{B}$. Let $\boldsymbol{\varphi}^h : \Omega^h \to \mathbb{R}^{n_{\text{dim}}}$ be a piecewise (tri)-bilinear isoparametric interpolation of the deformation $\boldsymbol{\varphi}(\boldsymbol{X})$ for $\boldsymbol{X} \in \Omega$, that is, at the element Ω_e^h we have

$$\boldsymbol{\varphi}_e^h(\boldsymbol{X}) = \sum_{A=1}^{n_{\text{node}}} (\boldsymbol{X}_A + \boldsymbol{d}_A) N^A \circ \hat{\boldsymbol{X}}^{-1} \tag{2.1}$$

where $\boldsymbol{X} = \hat{\boldsymbol{X}}(\boldsymbol{\xi})$ denotes the isoparametric map $\hat{\boldsymbol{X}} : \square \to \Omega_e^h$ from the parent domain $\square := [-1, 1]^{n_{\text{dim}}}$. Here, the vectors $\boldsymbol{d}_A \in \mathbb{R}^{n_{\text{dim}}}$ denote the unknown n_{node} nodal displacements ($n_{\text{node}} = 4, 8$ for 2D and 3D, respectively), $\boldsymbol{X}_A \in \mathbb{R}^{n_{\text{dim}}}$ are the nodal reference coordinates, and N^A are the standard isoparametric shape functions, that is,

$$N^A(\boldsymbol{\xi}) := \frac{1}{4}(1 + \xi^A \xi)(1 + \eta^A \eta) \,, \quad \text{for } \boldsymbol{\xi} = (\xi, \eta) \in \square \,, \tag{2.2}$$

in 2D, and

$$N^A(\boldsymbol{\xi}) := \frac{1}{8}(1 + \xi^A \xi)(1 + \eta^A \eta)(1 + \zeta^A \zeta) \,, \quad \text{for } \boldsymbol{\xi} = (\xi, \eta, \zeta) \in \square \,, \tag{2.3}$$

in 3D, where (ξ^A, η^A) and (ξ^A, η^A, ζ^A) for $A = 1, n_{\text{node}}$ are the vertices of the parent domain $\square$.

Our point of departure is the three-step procedure described in SIMO, ARMERO & TAYLOR [1993] for the construction of an additive enhancement of the deformation gradient $\boldsymbol{F} := \text{GRAD}_X \boldsymbol{\varphi}$ at the element level. This procedure results in the expression

$$\boldsymbol{F} = \underbrace{\text{GRAD}_X \boldsymbol{\varphi}^h}_{conforming} + \underbrace{\tilde{\boldsymbol{F}}}_{enhanced} \,, \tag{2.4}$$

with the enhanced part $\tilde{\boldsymbol{F}}$ given by

$$\tilde{\boldsymbol{F}} = \boldsymbol{F}_o\, \tilde{\mathbb{F}} \quad \text{with} \quad \tilde{\mathbb{F}} = \frac{j_o}{j} \boldsymbol{J}_o\, \mathbb{F}\, \boldsymbol{J}_o^{-1} \,. \tag{2.5}$$

Here, $\boldsymbol{J}_o$ denotes the Jacobian of the isoparametric map $\boldsymbol{X} = \hat{\boldsymbol{X}}(\boldsymbol{\xi})$ at the centroid, i.e.,

$$\boldsymbol{J} = \boldsymbol{J}(\boldsymbol{\xi}) := \frac{\partial \hat{\boldsymbol{X}}}{\partial \boldsymbol{\xi}} \,, \quad \boldsymbol{J}_o = \boldsymbol{J}(\boldsymbol{\xi})\Big|_{\boldsymbol{\xi}=\boldsymbol{0}} \tag{2.6}$$

with determinants denoted by

$$j = j(\boldsymbol{\xi}) := \det \boldsymbol{J}(\boldsymbol{\xi}) \,, \quad j_o = j(\boldsymbol{\xi})\Big|_{\boldsymbol{\xi}=\boldsymbol{0}} \,, \tag{2.7}$$

and $\boldsymbol{F}_o$ denotes the conforming part of the deformation gradient at the centroid

$$\boldsymbol{F}_o \equiv \text{GRAD}_0 \boldsymbol{\varphi}^h := \text{GRAD}_X \boldsymbol{\varphi}^h\Big|_{\boldsymbol{\xi}=\boldsymbol{0}} \,, \tag{2.8}$$

Note that the presence of $\boldsymbol{F}_o$ in (2.5) assures that the final deformation gradient (and thus the final finite element formulation) exhibits the proper transformation properties under change of observer, leading then to an *objective* formulation. The enhanced interpolations $\mathbb{F} = \mathbb{F}(\boldsymbol{\xi})$ are defined in the parent domain $\square$, and assumed of the form

$$\mathbb{F}(\boldsymbol{\xi}) = \sum_{I=1}^{n_{\text{enh}}} \mathbb{F}^I(\boldsymbol{\xi})\; \Gamma_I \,, \tag{2.9}$$

with n_{enh} enhanced parameters $\Gamma_I \in \mathbb{R}$ $(I = 1, n_{\text{enh}})$. The notation

$$\text{GRAD}_0[\cdot] := \text{GRAD}_X[\cdot]\Big|_{\boldsymbol{\xi}=0} \tag{2.10}$$

and

$$\tilde{\mathbb{F}}^I := \frac{j_o}{j} \boldsymbol{J}_o \mathbb{F}^I \boldsymbol{J}_o^{-1} \qquad I = 1, n_{\text{enh}} \tag{2.11}$$

will be used in the forthcoming developments.

With this notation in hand, the original Q1/E4 element is recovered as

$$\mathbb{F} = \Gamma_1 \begin{bmatrix} \xi & 0 \\ 0 & 0 \end{bmatrix} + \Gamma_2 \begin{bmatrix} 0 & 0 \\ \xi & 0 \end{bmatrix} + \Gamma_3 \begin{bmatrix} 0 & \eta \\ 0 & 0 \end{bmatrix} + \Gamma_4 \begin{bmatrix} 0 & 0 \\ 0 & \eta \end{bmatrix} \tag{2.12}$$

for the (unknown) enhanced parameters $\Gamma_I \in \mathbb{R}$ $(I = 1, 4)$ in plane strain problems, and similarly for the Q1/E9 brick in 3D. The QM1/E12 element is obtained by adding the three extra volumetric modes

$$\mathbb{F}_{10,11,12} = \Gamma_{10} \begin{bmatrix} \xi\eta & 0 & 0 \\ 0 & \xi\eta & 0 \\ 0 & 0 & \xi\eta \end{bmatrix} + \Gamma_{11} \begin{bmatrix} \xi\zeta & 0 & 0 \\ 0 & \xi\zeta & 0 \\ 0 & 0 & \xi\zeta \end{bmatrix} + \Gamma_{12} \begin{bmatrix} \eta\zeta & 0 & 0 \\ 0 & \eta\zeta & 0 \\ 0 & 0 & \eta\zeta \end{bmatrix} \tag{2.13}$$

together with a modification of the isoparametric gradients of the conforming part; see SIMO, ARMERO & TAYLOR [1993] for details. It is to be noted that the elements proposed in SIMO & ARMERO [1991] are based on an enhancement of this form. In fact, combining (2.5) and (2.12), we can write

$$\tilde{\boldsymbol{F}} = \sum_{I=1}^{2} \boldsymbol{\alpha}_I \otimes \boldsymbol{G}^I \,, \tag{2.14}$$

where $\boldsymbol{\alpha}_I := \boldsymbol{F}_o \boldsymbol{\Gamma}_I \in \mathbb{R}^{n_{\rm dim}}$ $(I = 1, 2)$ with

$$\boldsymbol{\Gamma}_1 := \begin{bmatrix} \Gamma_1 \\ \Gamma_2 \end{bmatrix} \,, \qquad \boldsymbol{\Gamma}_2 := \begin{bmatrix} \Gamma_3 \\ \Gamma_4 \end{bmatrix} \,, \tag{2.15}$$

and $\boldsymbol{G}^I = \frac{j_o}{j(\boldsymbol{\xi})} \boldsymbol{J}_o^{-T} \mathrm{GRAD}_\xi \hat{N}^I$ $(I = 1, 2)$ where

$$\hat{N}^1 = \tfrac{1}{2}(\xi^2 - 1) \quad \text{and} \quad \hat{N}^2 = \tfrac{1}{2}(\eta^2 - 1) \,, \tag{2.16}$$

i.e. the Wilson's shape functions. Similar construction holds for the enhanced Q1/E9 brick in 3D, as proposed in this last reference.

Two modifications of the above enhancement procedure are proposed herein:

i. *Option I.* We first consider the symmetrization of (2.12), that is,

$$\mathbb{F} = \Gamma_1 \begin{bmatrix} \xi & 0 \\ 0 & 0 \end{bmatrix} + \Gamma_2 \begin{bmatrix} 0 & \xi \\ \xi & 0 \end{bmatrix} + \Gamma_3 \begin{bmatrix} 0 & \eta \\ \eta & 0 \end{bmatrix} + \Gamma_4 \begin{bmatrix} 0 & 0 \\ 0 & \eta \end{bmatrix} \,, \tag{2.17}$$

and similarly for 3D. We denote the resulting finite elements by Q1/ES4 and Q1/ES9, respectively, and QM1/ES12 if the extra volumetric modes (2.13) are added.

ii. *Option II.* Numerical experiments show that the above modification suppresses the hourglass modes that appear for the Q1/E4 quad in compression. However, a stiff response of the element has been observed in bending dominated problems, as reported in Section 4.3. To avoid this drawback, the following basis of the enhanced deformation gradient is considered

$$\mathbb{F} = \Gamma_1 \begin{bmatrix} \xi & 0 \\ 0 & 0 \end{bmatrix} + \Gamma_2 \begin{bmatrix} 0 & \xi \\ 0 & 0 \end{bmatrix} + \Gamma_3 \begin{bmatrix} 0 & 0 \\ \eta & 0 \end{bmatrix} + \Gamma_4 \begin{bmatrix} 0 & 0 \\ 0 & \eta \end{bmatrix} \,, \tag{2.18}$$

and similarly for the three dimensional case. Furthermore, it has been observed numerically that the resulting elements lead to improved results in general distorted reference configurations if the transformation rule (2.5) is replaced by

$$\tilde{\mathbb{F}} = \frac{j_o}{j} \boldsymbol{J}_o^{-T} \, \mathbb{F} \, \boldsymbol{J}_o^{-1} \,, \tag{2.19}$$

We consider then this transformation in what follows for this enhancement, so (2.11) is modified accordingly for this case, leading to $\tilde{\mathbb{F}}^I := \frac{j_o}{j} \boldsymbol{J}_o^{-T} \mathbb{F}^I \boldsymbol{J}_o^{-1}$. The enhanced interpolations (2.18) are the transpose of the original (2.12), so the full symmetrization of the Q1/ES4 element is not required. The resulting finite elements are denoted by Q1/ET4 and Q1/ET9 for 2 and 3 dimensional problems, respectively, and QM1/ET12 is the extra volumetric modes (2.13) are added.

It is important to note that for both options, the resulting enhanced deformation gradient $\tilde{\boldsymbol{F}}$ cannot be written as the sum of the rank-one enhancements as in (2.14). As it is seen in the next section, this fact leads to a numerical implementation involving non-sparse matrices in the enhancement contributions, contrary to the original formulation in SIMO & ARMERO [1992] based on (2.15).

Remark 2.1.

In the same way, we consider the Q1/ES5 enhanced quad for axisymmetric analyses defined by

$$\mathbb{F} = \Gamma_1 \begin{bmatrix} \xi - \bar{\xi} & 0 & 0 \\ 0 & 0 & 0 \\ 0 & 0 & 0 \end{bmatrix} + \Gamma_2 \begin{bmatrix} 0 & \xi - \bar{\xi} & 0 \\ \xi - \bar{\xi} & 0 & 0 \\ 0 & 0 & 0 \end{bmatrix} + \Gamma_3 \begin{bmatrix} 0 & \eta - \bar{\eta} & 0 \\ \eta - \bar{\eta} & 0 & 0 \\ 0 & 0 & 0 \end{bmatrix}$$
$$+ \Gamma_4 \begin{bmatrix} 0 & 0 & 0 \\ 0 & \eta - \bar{\eta} & 0 \\ 0 & 0 & 0 \end{bmatrix} + \Gamma_5 \begin{bmatrix} 0 & 0 & 0 \\ 0 & 0 & 0 \\ 0 & 0 & \xi\eta \frac{j(\boldsymbol{\xi})}{j_0 R(\boldsymbol{\xi})} \end{bmatrix}, \tag{2.20}$$

the symmetrization of the original enhancement, where $\bar{\xi}$ and $\bar{\eta}$ are given by

$$\bar{\xi} = \frac{1}{\int_\square R(\boldsymbol{\xi}) d\xi d\eta} \int_\square \xi \, R(\boldsymbol{\xi}) d\xi d\eta \quad \text{and} \quad \bar{\eta} = \frac{1}{\int_\square R(\boldsymbol{\xi}) d\xi d\eta} \int_\square \eta \, R(\boldsymbol{\xi}) d\xi d\eta \,, \tag{2.21}$$

as proposed in SIMO & ARMERO [1993]. The enhanced interpolations

$$\mathbb{F} = \Gamma_1 \begin{bmatrix} \xi - \bar{\xi} & 0 & 0 \\ 0 & 0 & 0 \\ 0 & 0 & 0 \end{bmatrix} + \Gamma_2 \begin{bmatrix} 0 & \xi - \bar{\xi} & 0 \\ 0 & 0 & 0 \\ 0 & 0 & 0 \end{bmatrix} + \Gamma_3 \begin{bmatrix} 0 & 0 & 0 \\ \eta - \bar{\eta} & 0 & 0 \\ 0 & 0 & 0 \end{bmatrix}$$
$$+ \Gamma_4 \begin{bmatrix} 0 & 0 & 0 \\ 0 & \eta - \bar{\eta} & 0 \\ 0 & 0 & 0 \end{bmatrix} + \Gamma_5 \begin{bmatrix} 0 & 0 & 0 \\ 0 & 0 & 0 \\ 0 & 0 & \xi\eta \frac{j(\boldsymbol{\xi})}{j_0 R(\boldsymbol{\xi})} \end{bmatrix},$$

transpose of the original Q1/E5 enhancements, define the Q1/ET5 element. ■

For later use, we introduce the following notation for the finite element spaces associated to the interpolations described in this section. Denote by $\mathcal{U}^h$ the finite element space

$$\mathcal{U}^h := \left\{ \boldsymbol{\varphi}^h \text{ given by (2.1) for } \boldsymbol{d}_A \in \mathbb{R}^{n_{\text{dim}}} \ (A=1,n_{\text{node}}) \quad \text{and} \quad \boldsymbol{\varphi}^h = \boldsymbol{\varphi}\Big|_{\Gamma^h_{\boldsymbol{\varphi}}} \right\} , \tag{2.22}$$

for imposed essential boundary conditions $\bar{\boldsymbol{\varphi}}$ on on $\Gamma^h_{\boldsymbol{\varphi}} \subset \partial\Omega^h$. We denote by $\mathcal{U}^h_o$ the associated linear space of test functions satisfying homogeneous boundary conditions on $\Gamma^h_{\boldsymbol{\varphi}}$. Similarly, we introduce the linear space

$$\tilde{\mathcal{F}}^h = \left\{ \tilde{\mathbb{F}} \text{ given by the considerations above for } \Gamma_I \in \mathbb{R} \ (I=1,n_{\text{enh}}) \right\} , \tag{2.23}$$

where n_{enh} denotes the total number of assumed enhanced modes.

3. The Governing Equations

We develop in this section the finite element equations for the enhanced finite elements proposed in the previous section. We consider the model problem of finite hyperelasticity. The final equations are obtained in this case as the weak variational equations associated to a three field variational principle as proposed in Simo & Armero [1992] Practical issues related to the numerical linearization, including the consistent linearization, are described in Section 3.2.

3.1. The enhanced three-field variational formulation

Consider the case of a hyperelastic material characterized by a stored energy function $W = W(\boldsymbol{X}, \boldsymbol{F})$ in terms of the deformation gradient $\boldsymbol{F}$. This function is assumed to satisfy, by frame indifference,

$$W(\boldsymbol{X}, \boldsymbol{F}) = \hat{W}(\boldsymbol{X}, \boldsymbol{C}) , \quad \text{where} \quad \boldsymbol{C} := \boldsymbol{F}^T \boldsymbol{F} , \tag{3.1}$$

for all $\boldsymbol{F} \in \mathrm{GL}^{n_{\text{dim}}}_+$, the group of $n_{\text{dim}} \times n_{\text{dim}}$ matrices with positive determinant. The nominal stresses (first Piola-Kirchhoff stress tensor) $\boldsymbol{P}$ are then given by the standard expression

$$\boldsymbol{P} = \partial_{\boldsymbol{F}} W . \tag{3.2}$$

At the discrete level, we introduce an interpolation of these stresses $\boldsymbol{P}^h \in \mathcal{P}^h$, for some interpolation linear space, left undefined at this stage.

In this context, consider a Hu-Washizu type variational formulation of the nonlinear elastic boundary value problem involving the deformation $\boldsymbol{\varphi}^h \in \mathcal{U}^h$, enhanced deformation gradient $\tilde{\mathbb{F}} \in \tilde{\mathcal{F}}^h$ and the nominal stresses $\boldsymbol{P}^h \in \mathcal{P}^h$, defined by the three-field functional

$$\Pi(\boldsymbol{\varphi}^h, \tilde{\mathbb{F}}, \boldsymbol{P}^h) := \int_{\Omega^h} \left[W(\boldsymbol{F}^h) + \boldsymbol{P}^h : \left[\text{GRAD}_X \boldsymbol{\varphi}^h - \boldsymbol{F}^h \right] \right] d\Omega + \Pi_{ext}(\boldsymbol{\varphi}^h) \tag{3.3}$$

where $\boldsymbol{F}^h = \boldsymbol{F}^h(\boldsymbol{\varphi}^h, \tilde{\mathbb{F}})$ is given by expression (2.12). Here, Π_{ext} denotes the potential energy of the external loading, assumed conservative, and given by

$$\Pi_{ext}(\boldsymbol{\varphi}^h) = -\int_{\Omega^h} \boldsymbol{B} \cdot \boldsymbol{\varphi}^h d\Omega - \int_{\Gamma^h} \boldsymbol{T} \cdot \boldsymbol{\varphi}^h d\Gamma$$

for a nominal body force $\boldsymbol{B}: \Omega^h \to \mathbb{R}^{n_{\text{dim}}}$ and imposed nominal surface traction $\boldsymbol{T}: \Gamma_T^h \to \mathbb{R}^{n_{\text{dim}}}$ over part of the boundary $\Gamma_{\boldsymbol{T}}^h \subset \partial\Omega^h$. The usual assumptions

$$\overline{\Gamma_{\boldsymbol{\varphi}} \cup \Gamma_{\boldsymbol{T}}} = \partial\Omega\,, \qquad \text{and} \qquad \Gamma_{\boldsymbol{\varphi}} \cup \Gamma_{\boldsymbol{T}} = \emptyset \tag{3.4}$$

are considered. Without loss of generality, the explicit dependence of $W(\boldsymbol{X}, \cdot)$ on the the particle $\boldsymbol{X}$ (inhomogeneity) has been omitted in (3.3) and in the forthcoming considerations. Inserting (2.12) in (3.3), the latter can be written

$$\Pi(\boldsymbol{\varphi}^h, \tilde{\mathbb{F}}, \boldsymbol{P}^h) := \int_{\Omega^h} \left[W(\boldsymbol{F}^h) - \boldsymbol{P}^h : \tilde{\boldsymbol{F}}^h \right] d\Omega + \Pi_{ext}(\boldsymbol{\varphi}^h) \tag{3.5}$$

where $\tilde{\boldsymbol{F}}^h = \tilde{\boldsymbol{F}}^h(\boldsymbol{\varphi}^h, \tilde{\mathbb{F}})$ is given explicitly in equation (2.5), and considerations that follow.

Evaluation of the first variation of the functional (3.3) lead after standard manipulations to the following set of three weak equations

$$\int_{\Omega^h} \left[\partial_{\boldsymbol{F}} W : [\text{GRAD}_X \delta\boldsymbol{\varphi}^h + \text{GRAD}_0 \delta\boldsymbol{\varphi}^h \; \tilde{\mathbb{F}}] - \boldsymbol{P}^h : \text{GRAD}_0 \delta\boldsymbol{\varphi}^h \; \tilde{\mathbb{F}} \right] d\Omega$$

$$-G_{ext}(\delta\boldsymbol{\varphi}^h) = 0 \quad \forall\, \delta\boldsymbol{\varphi}^h \in \mathcal{U}_o^h\,, \tag{3.6.a}$$

$$\int_{\Omega^h} \left[\partial_{\boldsymbol{F}} W - \boldsymbol{P}^h \right] : \boldsymbol{F}_o \; \delta\tilde{\mathbb{F}} \; d\Omega = 0 \quad \forall\, \delta\tilde{\mathbb{F}} \in \tilde{\mathcal{F}}^h\,, \tag{3.6.b}$$

$$\int_{\Omega^h} \delta\boldsymbol{P}^h : \boldsymbol{F}_o \; \tilde{\mathbb{F}} \; d\Omega = 0 \quad \forall\, \delta\boldsymbol{P}^h \in \mathcal{P}^h\,. \tag{3.6.c}$$

We next impose the condition

$$\int_{\Omega^h} \boldsymbol{P}^h : \text{GRAD}_0 \boldsymbol{\varphi}^h \; \tilde{\mathbb{H}} \; d\Omega = 0 \qquad \forall \boldsymbol{P}^h \in \mathcal{P}^h\,, \;\; \forall \mathbb{H} \in \tilde{\mathcal{F}}^h\,, \tag{3.7}$$

for any $\boldsymbol{\varphi}^h \in \mathcal{U}^h$. Since, any function $\delta\boldsymbol{\varphi}^h$ in the linear space $\mathcal{U}_o^h$ can be expressed as the difference of two functions of the affine space $\mathcal{U}^h$, satisfaction of the condition (3.7) also implies its satisfaction for any $\delta\boldsymbol{\varphi}^h \in \mathcal{U}_o^h$. Condition (3.7) can be understood as generalized orthogonality conditions between the linear spaces $\mathcal{P}^h$ and $\tilde{\mathcal{F}}^h$, depending on the space $\text{GRAD}_0 \mathcal{U}_o^h$. We note that the imposition of the condition

$$\int_{\Omega_e^h} \tilde{\mathbb{F}} \; d\Omega = 0 \qquad \forall \tilde{\mathbb{F}} \in \tilde{\mathcal{F}}^h\,, \tag{3.8}$$

on the enhanced interpolations $\tilde{\mathbb{F}}$ for each element Ω_e^h, assures the satisfaction of (3.7) for at least piecewise constant nominal stresses ($\boldsymbol{P}^h|_{\Omega_e^h} = constant$), as a simple calculation shows. Condition (3.8) implies then the satisfaction of the patch test in nominal stresses and, by assuming the transformation $(2.5)_2$ or the alternative transformation (2.19), it reduces to

$$\int_{\square} \mathbb{F}\, d\square = 0\,. \tag{3.9}$$

This last condition is satisfied by all the interpolations introduced in Section 2.

Making use of the conditions (3.7), the weak equations (3.6) reduce to

$$\int_{\Omega^h} \partial_{\boldsymbol{F}} W\colon \left[\text{GRAD}_X \delta\boldsymbol{\varphi}^h + \text{GRAD}_0 \delta\boldsymbol{\varphi}^h\ \tilde{\mathbb{F}}\right]\ d\Omega - G_{ext}(\delta\boldsymbol{\varphi}^h) = 0 \quad \forall\ \delta\boldsymbol{\varphi}^h \in \mathcal{U}_o^h\,, \tag{3.10.a}$$

$$\int_{\Omega_e^h} \partial_{\boldsymbol{F}} W\colon \boldsymbol{F}_o\ \delta\tilde{\mathbb{F}}\ d\Omega = 0 \quad \forall\ \delta\tilde{\mathbb{F}} \in \tilde{\mathcal{F}}^h\,. \tag{3.10.b}$$

with (3.6.c) satisfied exactly. In writing equation (3.10.b) we have made explicit use of the piecewise form of the interpolations $\tilde{\mathbb{F}}$ at each element Ω_e^h. As described in the following section, this observation carries important consequences in the numerical implementation of the proposed elements. As occurs in the original enhanced formulations, the interpolated stress field $\boldsymbol{P}^h$ drops from the formulation, and does not need to be specified explicit, being recovered as a post-processing if required. See SIMO & RIFAI [1991] for variationally consistent stress recoveries.

3.2. The finite element equations

An efficient numerical implementation of the weak equations (3.10) is accomplished by expressions the different contributions in terms of objects in the current configuration $\boldsymbol{\varphi}^h(\Omega^h)$. This leads to sparse matrices in the most part. To this purpose, we introduce the Kirchhoff stresses

$$\boldsymbol{\tau} := \partial_{\boldsymbol{F}} W(\boldsymbol{F}^h)\ \boldsymbol{F}^{h^T} \tag{3.11}$$

which are symmetric after a simple calculation using (3.1) shows. The vector notation

$$\hat{\boldsymbol{\tau}} := [\,\tau^{11} \quad \tau^{22} \quad \tau^{12}\,] \tag{3.12}$$

for 2D (and similarly for 3D) is introduced. We also consider the notation

$$\overline{\text{GRAD}_X}[\cdot] := \text{GRAD}_X[\cdot] + \tilde{\mathbb{F}}^T \text{GRAD}_0[\cdot]\,, \quad \overline{\nabla}[\cdot] := \boldsymbol{F}^{-T}\overline{\text{GRAD}_X}[\cdot]\,, \tag{3.13}$$

and

$$\nabla_o[\cdot] := \boldsymbol{F}_o^{-T}\text{GRAD}_0[\cdot]\ \left(= \overline{\nabla}[\cdot]\Big|_{\boldsymbol{\xi}=0}\right), \tag{3.14}$$

following as close as possible the notation in SIMO, ARMERO & TAYLOR [1993].

i. *The finite element residual.* With this notation at hand, the weak equations (3.10) lead to a the following set of finite element equations

$$\boxed{\begin{aligned} \boldsymbol{R} &:= \mathop{\mathbf{A}}_{e=1}^{n_{\text{elem}}} \int_{\Omega_e^h} \boldsymbol{b}^T \hat{\boldsymbol{\tau}}\; d\Omega - \boldsymbol{f}_{ext} = 0 \\ \boldsymbol{r}_{e,enh} &:= \int_{\Omega_e^h} \boldsymbol{g}^T \hat{\boldsymbol{\tau}}\; d\Omega = 0 \end{aligned}} \tag{3.15}$$

The linearized strain operator $\boldsymbol{b}$ is defined as

$$\boldsymbol{b} = \left[\, \boldsymbol{b}^1 \quad \dots \quad \boldsymbol{b}^{n_{\text{node}}} \,\right] , \quad \text{where} \quad \boldsymbol{b}^A = \begin{bmatrix} N^A_{\bar{1}} & 0 \\ 0 & N^A_{\bar{2}} \\ N^A_{\bar{2}} & N^A_{\bar{1}} \end{bmatrix} \quad \text{for } A = 1, n_{\text{node}} , \tag{3.16}$$

where the $[N^A_{\bar{1}}\ N^A_{\bar{2}}]^T = \overline{\nabla} N^A$. The linearized enhanced strain operator is defined as

$$\boldsymbol{g} = \left[\, \boldsymbol{g}^1 \dots \boldsymbol{g}^{n_{\text{enh}}} \,\right] , \quad \text{where} \quad \boldsymbol{g}^I = \begin{bmatrix} \mathrm{G}^I_{11} \\ \mathrm{G}^I_{22} \\ \mathrm{G}^I_{12} + \mathrm{G}^I_{21} \end{bmatrix} \quad \text{for } I = 1, n_{\text{enh}} , \tag{3.17}$$

where we have introduced the notation

$$\mathbb{G}^I = \begin{bmatrix} \mathrm{G}^I_{11} & \mathrm{G}^I_{12} \\ \mathrm{G}^I_{21} & \mathrm{G}^I_{22} \end{bmatrix} := \boldsymbol{F}_o\ \tilde{\mathbb{F}}^I\ \boldsymbol{F}^{-1} . \tag{3.18}$$

ii. *The stiffness matrix.* The set of nonlinear equations (3.15) are solved using a Newton-Raphson scheme, leading to the linearized equations

$$\begin{bmatrix} \boldsymbol{K}_{dd} & \boldsymbol{K}_{da} \\ \boldsymbol{K}_{ad} & \boldsymbol{K}_{aa} \end{bmatrix}^{(k)} \begin{bmatrix} \Delta \boldsymbol{d} \\ \Delta \boldsymbol{\Gamma} \end{bmatrix} = \begin{bmatrix} \boldsymbol{R}^{(k)} \\ \boldsymbol{r}^{(k)}_{enh} \end{bmatrix} , \tag{3.19}$$

for the increments of the nodal displacements $\Delta \boldsymbol{d} = \boldsymbol{d}^{(k+1)} - \boldsymbol{d}^{(k)}$ and and enhanced parameters $\Delta \boldsymbol{\Gamma} = \boldsymbol{\Gamma}^{(k+1)} - \boldsymbol{\Gamma}^{(k)}$, at iteration (k).

As usual, the tangent matrix consists of a material and geometric part,

$$\begin{bmatrix} \boldsymbol{K}_{dd} & \boldsymbol{K}_{da} \\ \boldsymbol{K}_{ad} & \boldsymbol{K}_{aa} \end{bmatrix} = \underbrace{\begin{bmatrix} \boldsymbol{K}_{m,dd} & \boldsymbol{K}_{m,da} \\ \boldsymbol{K}_{m,ad} & \boldsymbol{K}_{m,aa} \end{bmatrix}}_{material} + \underbrace{\begin{bmatrix} \boldsymbol{K}_{g,dd} & \boldsymbol{K}_{g,da} \\ \boldsymbol{K}_{g,ad} & \boldsymbol{K}_{g,aa} \end{bmatrix}}_{geometric} \tag{3.20}$$

The expressions for the element contributions to the material part can be written as

$$\left.\begin{aligned} \boldsymbol{K}^{AB}_{m,dd} &= \int_{\Omega^h_e} \boldsymbol{b}^{A^T}\ \mathbf{c}\ \boldsymbol{b}^B\ d\Omega \in \mathbb{R}^{n_{\text{dim}}\times n_{\text{dim}}}\ , && A,B=1,n_{\text{node}}\ , \\ \boldsymbol{K}^{IJ}_{m,aa} &= \int_{\Omega^h_e} \boldsymbol{g}^{I^T}\ \mathbf{c}\ \boldsymbol{g}^J\ d\Omega \in \mathbb{R}\ , && I,J=1,n_{\text{enh}}\ , \\ \boldsymbol{K}^{AJ}_{m,da} &= \int_{\Omega^h_e} \boldsymbol{b}^{A^T}\ \mathbf{c}\ \boldsymbol{g}^J\ d\Omega \in \mathbb{R}^{n_{\text{dim}}}\ , && A=1,n_{\text{node}}\ J=1,n_{\text{enh}}\ , \end{aligned}\right\} \tag{3.21}$$

where the spatial tangent $\mathbf{c}$ is given in components as

$$\mathbf{C} = 2\frac{\partial^2 W}{\partial \boldsymbol{C}^2} \qquad \text{and} \qquad c^{abcd} = F^a{}_A F^b{}_B F^c{}_C F^d{}_D C^{ABCD}\ , \tag{3.22}$$

with the corresponding matrix version following the standard procedure. The geometric contributions to the stiffness matrix are given by

$$\left.\begin{aligned} \boldsymbol{K}^{AB}_{g,dd} &= \left[\int_{\Omega^h_e} \overline{\nabla} N^A \cdot \boldsymbol{\tau} \overline{\nabla} N^B\ d\Omega\right] \mathbf{1}\ , && A,B=1,n_{\text{node}}\ , \\ \boldsymbol{K}^{IJ}_{g,aa} &= \int_{\Omega^h_e} \mathbb{G}^I\ \boldsymbol{\tau}\ :\ \mathbb{G}^J\ d\Omega\ , && I,J=1,n_{\text{enh}}\ , \\ \boldsymbol{K}^{AJ}_{g,da} &= \int_{\Omega^h_e} \left[\mathbb{G}^J\ \boldsymbol{\tau}\ \overline{\nabla} N^A + \boldsymbol{\tau}\ \mathbb{G}^{J^T}\ \nabla_o N^A\right]\ d\Omega\ , && A=1,n_{\text{node}}\ J=1,n_{\text{enh}}\ , \end{aligned}\right\} \tag{3.23}$$

where $\mathbf{1}$ is the $n_{\text{dim}} \times n_{\text{dim}}$ identity matrix. Note that for the hyperelastic problem under consideration, the stiffness matrix is symmetric (i.e., $\boldsymbol{K}_{ad} = \boldsymbol{K}^T_{da}$).

The enhanced parameters Γ_I $(I = 1, n_{\text{enh}})$ are defined independently for each element, allowing their elimination at the element level. The system (3.19) is then reduced by static condensation to

$$\boldsymbol{K}^{*,(k)} \Delta \boldsymbol{d} = \boldsymbol{R}^{*,(k)} \tag{3.24}$$

where the effective stiffness matrix $\boldsymbol{K}^*$ and effective residual $\boldsymbol{R}^{*,(k)}$ are defined as

$$\boldsymbol{K}^* := \mathop{\mathbf{A}}_{e=1}^{n_{\text{elem}}} \left[\boldsymbol{K}_{dd} - \boldsymbol{K}_{da}\boldsymbol{K}^{-1}_{aa}\boldsymbol{K}_{ad}\right]\ , \tag{3.25}$$

$$\boldsymbol{R}^* := \mathop{\mathbf{A}}_{e=1}^{n_{\text{elem}}} \left[\boldsymbol{R} - \boldsymbol{K}_{da}\boldsymbol{K}^{-1}_{aa}\boldsymbol{r}_{enh}\right]\ , \tag{3.26}$$

Here, the symbol $\mathbf{A}_{e=1}^{n_{\text{elem}}}$ denotes the assembly over the different elements, and all the arrays in the right-hand-side of these expressions refer to their elemental counterparts.

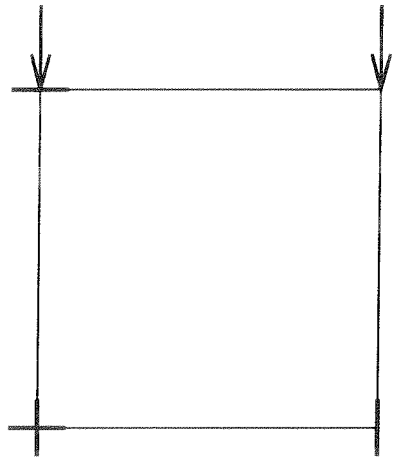

FIGURE 4.1. Boundary conditions for the constrained single element test, plane strain.

4. Representative Numerical Simulations

The goal of this section is to assess numerically the performance of the enhanced finite elements proposed herein. A number of benchmark numerical simulations are presented, involving plane strain, axisymmetric and three dimensional problems with elastic and elasto-plastic models. Comparisons with previous and alternative enhanced formulations are included.

4.1. Homogeneous compression tests

Homogeneous compression tests are performed with different configurations. First, tests involving a single element are performed under two different sets of boundary conditions. The results are reported in Section 4.1.1 and Section 4.1.2. Homogeneous compression tests with more general multi-element meshes are considered in Section 4.1.3.

4.1.1. Constrained single element test

We first consider the one element test described in WRIGGERS & REESE [1995]. The test consists of the homogeneous compression of a single bi-unit element under imposed displacement in plane strain conditions. The prescribed boundary conditions are depicted in Figure 4.1. A compressible Neo-Hookean hyperelastic model with the stored energy function

$$W = \frac{1}{4}\Lambda\,(J^2 - 1 - 2\ln J) + \frac{1}{2}\mu\,[\mathrm{tr}\boldsymbol{b} - 3] - \mu \ln J \tag{4.1}$$

is assumed. The material parameters $\Lambda = 10^5$ and $\mu = 20$ are considered, leading to a nearly incompressible response.

Static condensation of the enhanced degrees of freedom is performed at the element

a)

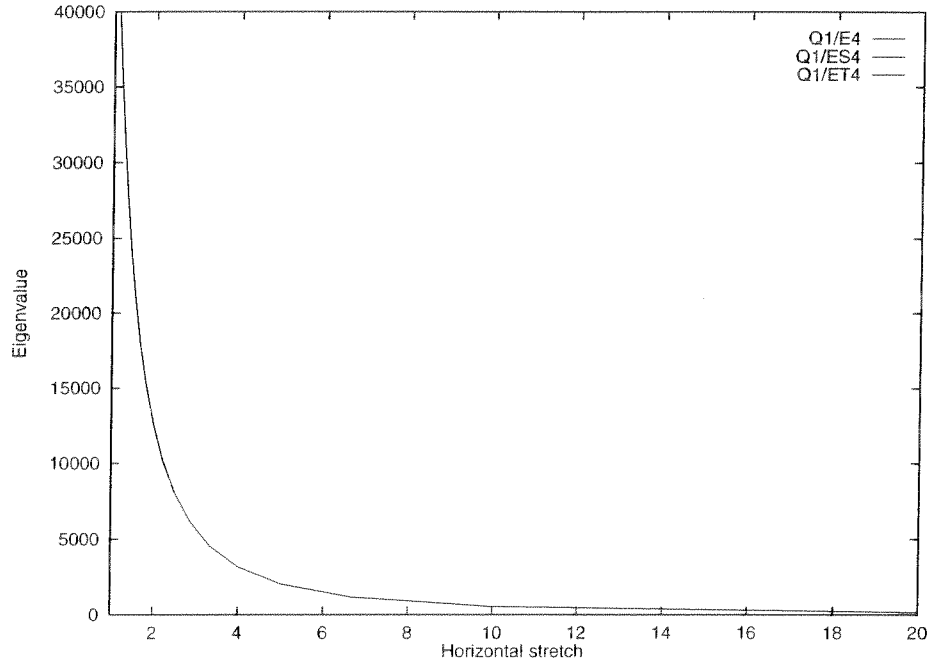

b)

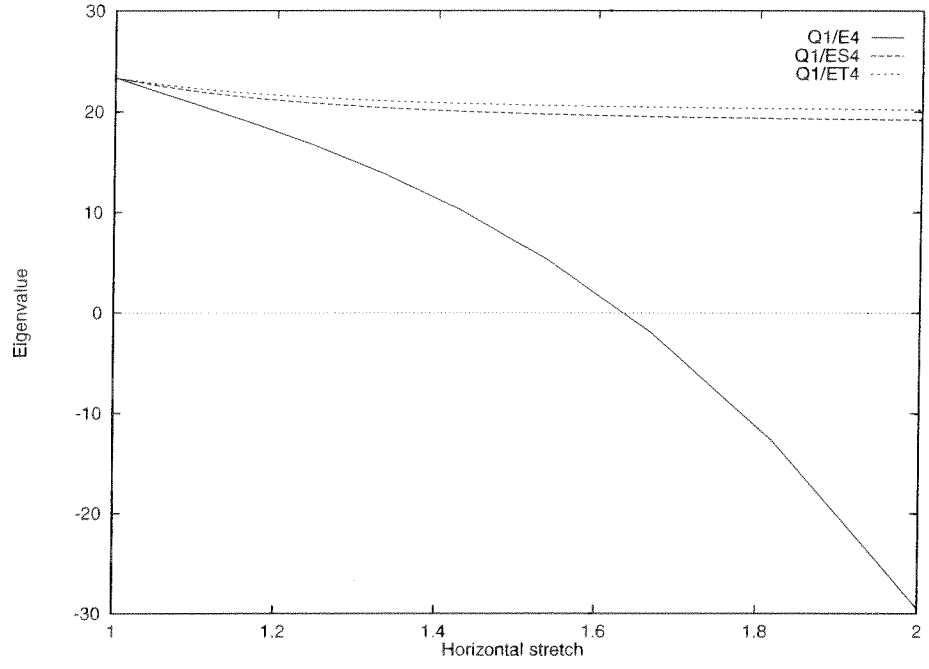

FIGURE 4.2. Constrained single element test. **a)** Eigenvalue corresponding to the stretching mode. **b)** Eigenvalue corresponding to the bending mode vs. horizontal stretch (different scales are used).

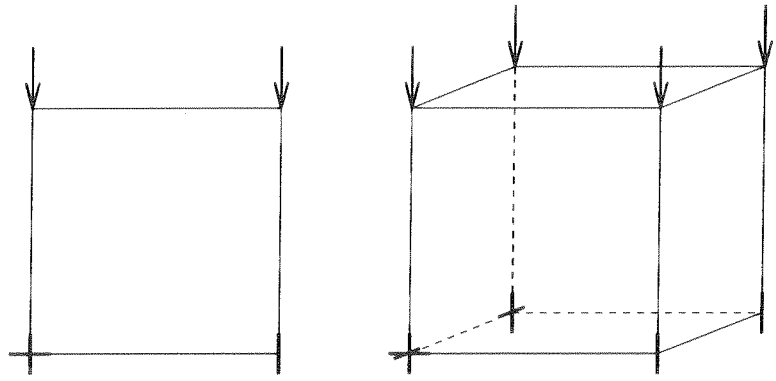

FIGURE 4.3. Boundary conditions for the unconstrained single element test. Plane strain (left) and three dimensional case (right).

level, leading to a total of two free degrees of freedom in this case. The two eigenvalues of the resulting linearized system for the original enhanced Q1/E4 and the newly proposed Q1/ES4 and Q1/ET4 quads are plotted versus the horizontal stretch λ_1 in Figure 4.2. More specifically, Figure 4.2.a depicts the eigenvalue ω_1 corresponding to the stretching mode, whereas Figure 4.2.b shows the second eigenvalue ω_2, associated to the bending mode. The analytical evaluation of the stiffness matrix presented in WRIGGERS & REESE [1994] detects the appearance of a negative eigenvalue for the Q1/E4 element at $\lambda_1 = 1.6344$ (39% compression) for this example. This eigenvalue is observed also in our numerical experiment. In contrast, no negative eigenvalues appear for the Q1/ES4 and Q1/ET4 elements. The eigenvalue ω_2 remains positive for all λ_1. The same eigenvalue ω_1, corresponding to the stretching mode, is observed for the Q1/E4, the Q1/ES4 and Q1/ET4 elements, as shown in Figure 4.2.a. This mode involves a constant strain which is exactly captured by all the elements, since all pass the patch test.

4.1.2. Unconstrained single element test

The test is repeated with the boundary conditions depicted in Figure 4.3. The upper left node is released in the horizontal direction, allowing the appearance of hourglass modes. The three dimensional counterpart of this problem is also considered; see Figure 4.3. The compressible Neo-Hookean hyperelastic model defined by the stored energy function

$$W = \frac{1}{2}\Lambda\,(\ln J)^2 + \frac{1}{2}\mu\,[\mathrm{tr}\boldsymbol{b} - 3] - \mu \ln J \tag{4.2}$$

is assumed in this case, with $\Lambda = 40000$ and $\mu = 80.2$, leading to nearly incompressible response. This problem has been considered previously in CRISFIELD et al [1995]. The element is compressed by an imposed displacement on the upper nodes. An eigenvalue evaluation is performed at the end of each increment on the *condensed element stiffness matrix.*

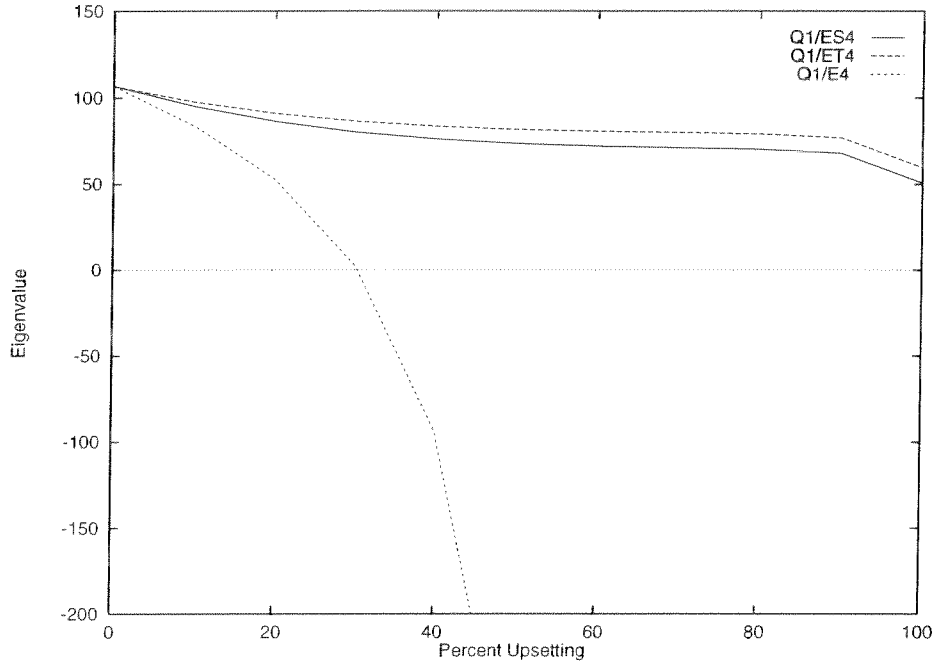

FIGURE 4.4. Unconstrained single element test. Eigenvalue of the bending mode orthogonal to the compression direction. ($\Lambda = 40000$, $\mu = 80.2$)

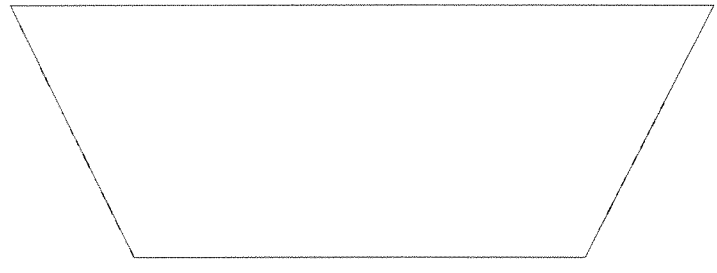

FIGURE 4.5. Constrained single element test. Hourglass mode with negative eigenvalue for the Q1/E4 element.

TABLE 4.1. Unconstrained single element test. Compression stage at which the first non-physical negative eigenvalue appears for different elements.

Element	% Compression
Q1/E4	32%
Q1/ES4	none
Q1/ET4	none
Q1/E4-C	28%
Q1/E4-U	64%

i. *The plane strain case.* The three zero eigenvalues corresponding to the rigid body modes (two translations and one rotation) are observed for the unloaded configuration and the three elements, Q1/E4, Q1/ES4 and Q1/ET4. Upon loading, only two eigenvalues remain zero. The eigenvalue corresponding to the infinitesimal rotation turns negative under compression (positive under tension), as expected from physical considerations. The next eigenvalue is plotted versus the imposed vertical stretch for the Q1/E4 and Q1/ES4 elements in Figure 4.4. The original Q1/E4 element exhibits a second negative eigenvalue at 32% compression. The associated eigenvector corresponds to the hourglass mode (bending mode) orthogonal to the compression direction. This eigenvector is shown in Figure 4.5. The same curves are obtained with either 2x2 or 3x3 Gaussian quadrature rules and the 5-point quadrature rule proposed in SIMO & ARMERO [1992] for this case involving an homogeneous deformation. The negative eigenvalue is indicated in the solution process with a the appearance of a negative pivot in a direct solution of the algebraic system of equations. This negative eigenvalue is not observed for the symmetrically enhanced Q1/ES4 element and the Q1/ET4 element at any stage of the loading process. In contrast, the Q1/ES4 and Q1/ET4 elements show the proper behavior in this single element compression test.

The performances of alternative enhanced formulations under plane strain compression are summarized in Table 4.1 for this benchmark problem. The element referred to as the Q1/E4-C involves the enhancement of the right Cauchy-Green tensor as

$$\boldsymbol{C} = \bar{\boldsymbol{C}} + \tilde{\boldsymbol{C}} \,, \tag{4.3}$$

whereas the Q1/E4-U element is based on an enhancement of the form

$$\boldsymbol{F} = \bar{\boldsymbol{F}} + \bar{\boldsymbol{R}}_0 \tilde{\boldsymbol{U}} \,. \tag{4.4}$$

Here, $\bar{\boldsymbol{C}} = \bar{\boldsymbol{F}}^T \bar{\boldsymbol{F}}$ is the compatible right Cauchy-Green tensor, and $\bar{\boldsymbol{R}}_0$ is the rotation tensor associated to the compatible deformation gradient $\bar{\boldsymbol{F}}$ at the center of the element. The enhanced parts $\tilde{\boldsymbol{C}}$ and $\tilde{\boldsymbol{U}}$ are symmetric enhancement tensors having the same form

as the Q1/ES4 enhancement tensor $\tilde{\boldsymbol{F}}$ in equation (2.17). All elements are numerically integrated with 3x3 point Gaussian integration rule. In the unloaded configuration all elements exhibit the same stiffness matrix, reducing in the infinitesimal case to the QM6 element presented in TAYLOR et al. [1976]. All the elements, except the proposed Q1/ES4 and Q1/ET4 quads, exhibit a non-physical negative eigenvalue at a certain stage.

ii. *The three dimensional case.* The same performances are observed in the three dimensional case. The six zero eigenvalues corresponding to rigid body motions in the unloaded configuration reduce to three upon loading. The three dimensional Q1/E9 element exhibits a negative eigenvalue corresponding to a three dimensional bending mode at 32% compression. A second negative eigenvalue appears at 44% compression, being related to a second three dimensional bending mode. The symmetric enhanced three dimensional Q1/ES9 and Q1/ET9 elements behave properly in this test. No negative eigenvalues associated with bending modes could be detected at any compression state. It is to be noted that a negative eigenvalue corresponding to a twisting deformation in three dimensions appears in both elements. This twisting mode with negative eigenvalue is also present in the regular non-enhanced three dimensional Q1 element, and is then not related to the enhancement of the element.

4.1.3. Multi-element homogeneous compression test

Homogeneous compression tests are performed with more general multi-element discretizations in plane strain. A 1×1 block is considered. Only the right half of the block is discretized using 200 Q1/ES4 elements. Symmetry boundary conditions are imposed along the vertical center line. The bottom of the block is restrained in the vertical direction only, with an imposed vertical displacement at the top. The 3×3 Gaussian quadrature rule is considered. The same material model as considered in the previous section, characterized by the stored energy function (4.2), with the same material properties $\Lambda = 40000.$ and $\mu = 80.2$, is assumed in this case.

The block is compressed to an homogeneous state of deformation. The load deflection curve is depicted in Figure 4.6. During the upsetting an eigenvalue calculation on the global equation system containing the enhancement degrees of freedom is performed after the convergence for each increment is achieved. Up to 49.6% compression all eigenvalues of the system remain positive. At this stage one eigenvalue turns negative indicating a physical bifurcation. The eigenvector associated to this eigenvalue corresponds to the first bulging mode as shown in Figure 4.7.a. Shortly after a second negative eigenvalue appears at a deformation stage of 49.76%. This eigenvalue corresponds to the second bulging mode shown in Figure 4.7.b. At a deformation stage of 56% compression the third negative eigenvalue appears. The corresponding eigenvector is shown in Figure 4.7.c. A fourth negative eigenvalue appears at 76% compression; the corresponding eigenvector is depicted in Figure 4.7.d. The next negative eigenvalue is obtained at 92% upsetting followed by

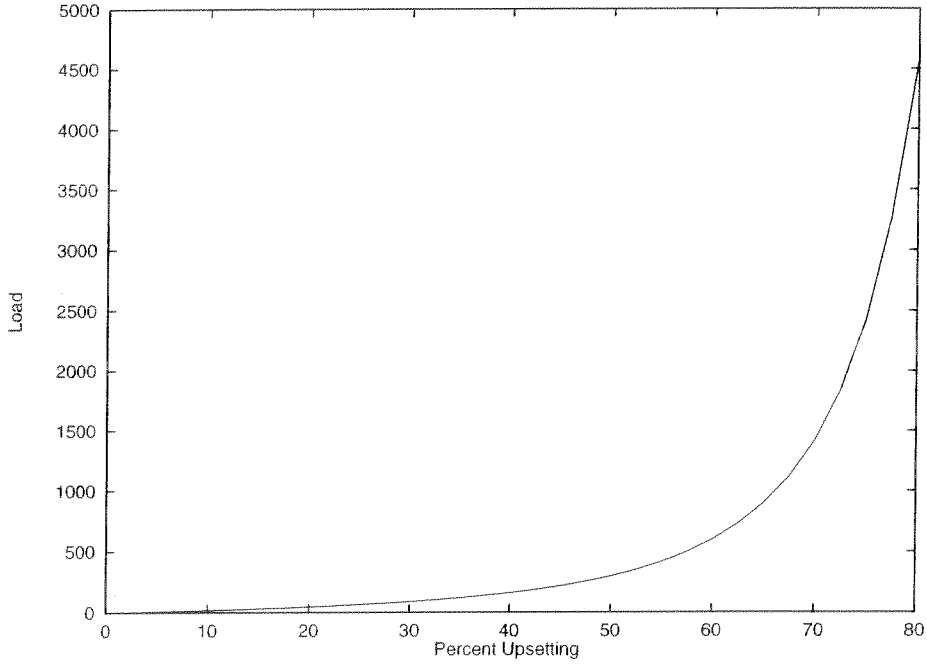

FIGURE 4.6. Load-deflection curve of the hyperelastic block computed with the Q1/ES4 and Q1/ET4 elements.

the sixth negative eigenvalue at 96%. At a deformation stage of 99% upsetting seven negative eigenvalues are present. All of them correspond to physical bulging patterns. No eigenvectors with negative eigenvalues showing hourglass patterns could be detected with the Q1/ES4 or Q1/ET4 elements.

TABLE 4.2. Material properties.

Bulk Modulus	κ	164.21	GPa
Shear Modulus	μ	80.1938	GPa
Initial Flow Stress	y_o	0.450	GPa
Saturation Flow Stress	y_∞	0.715	GPa
Saturation Exponent	δ	16.93	
Linear Hardening	H	0.12924	GPa

4.2. Upsetting of an elasto-plastic block

This example corresponds to the upsetting of an elasto-plastic block in plane strain. A square block of 6.35 $\times$ 6.35 mm^2 is considered. Only the right half of the block is discretized with 200 Q1/ES4 and Q1/ET4 element, respectively. Symmetry boundary

a)

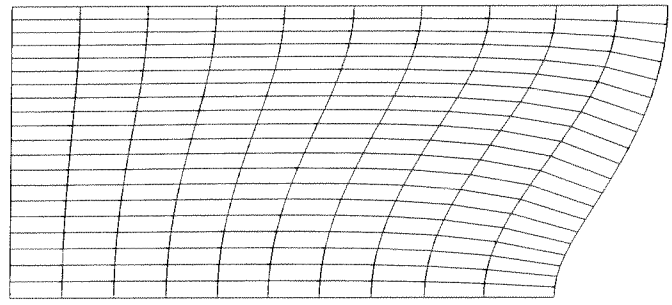

b)

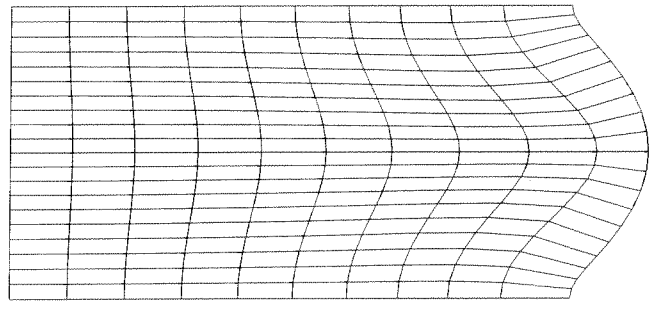

c)

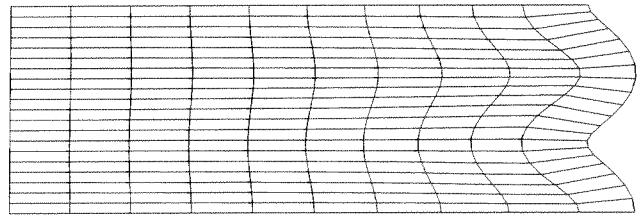

d)

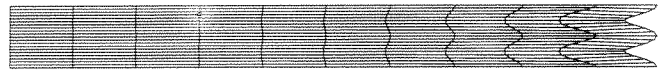

FIGURE 4.7. Bulging eigenvectors superposed on the deformed configuration of the rubber block at **a)** 49.60%, **b)** 49.76%, **c)** 56.%, **d)** 76.%, compression.

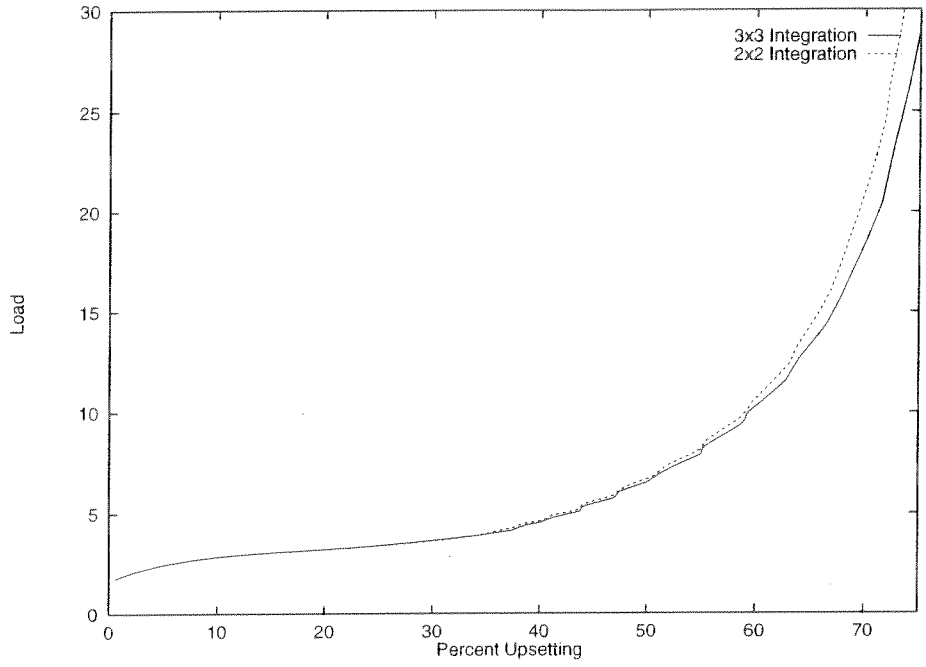

FIGURE 4.8. Load-deflection curve of the elasto plastic block, obtained with the Q1/ES4 element.

conditions are imposed along the vertical center line. The bottom of the block is restrained in the vertical and horizontal directions, leading to a non-homogeneous state of stress after loading. The block is loaded with an imposed displacement on the top base. A rigid surface with a frictional coefficient of 0.3 is located at the bottom to simulate a forming tool. In order to examine the influence of the quadrature rule, the integration is done by using the 2x2 point Gaussian integration rule, the 3x3 point Gaussian integration rule and the 5 point integration rule. The finite strain plasticity model based on the multiplicative decomposition of the deformation gradient described in SIMO & ARMERO [1992] is considered. The assumed material properties are summarized in Table 4.2.

The computed load-deflection curve for this case is depicted in Figure 4.8 for the 2x2 and 3x3 point Gaussian integration rules. The behavior of the element with 3x3 point Gaussian integration and the 5-point integration proposed in SIMO & ARMERO [1992] are nearly identical. Even though the influence of the quadrature rule in the load-deflection curve is negligible, significant differences are observed in the deformed geometry when using 2x2 or 3x3 point Gaussian quadratures, as becomes apparent in Figure 4.9. The solution obtained with the Q1/ES4 element is shown. The 3x3 point and the 5 point integration rules give again nearly identical results, and so it does the Q1/ET4 element.

Figure 4.9 depicts the deformed configuration of the block at 25%, 35%, 50% and 74% upsetting for the 2x2 and 3x3 point Gaussian integration rules. With both integration rules no hourglassing can be observed even under high compression. However, with the

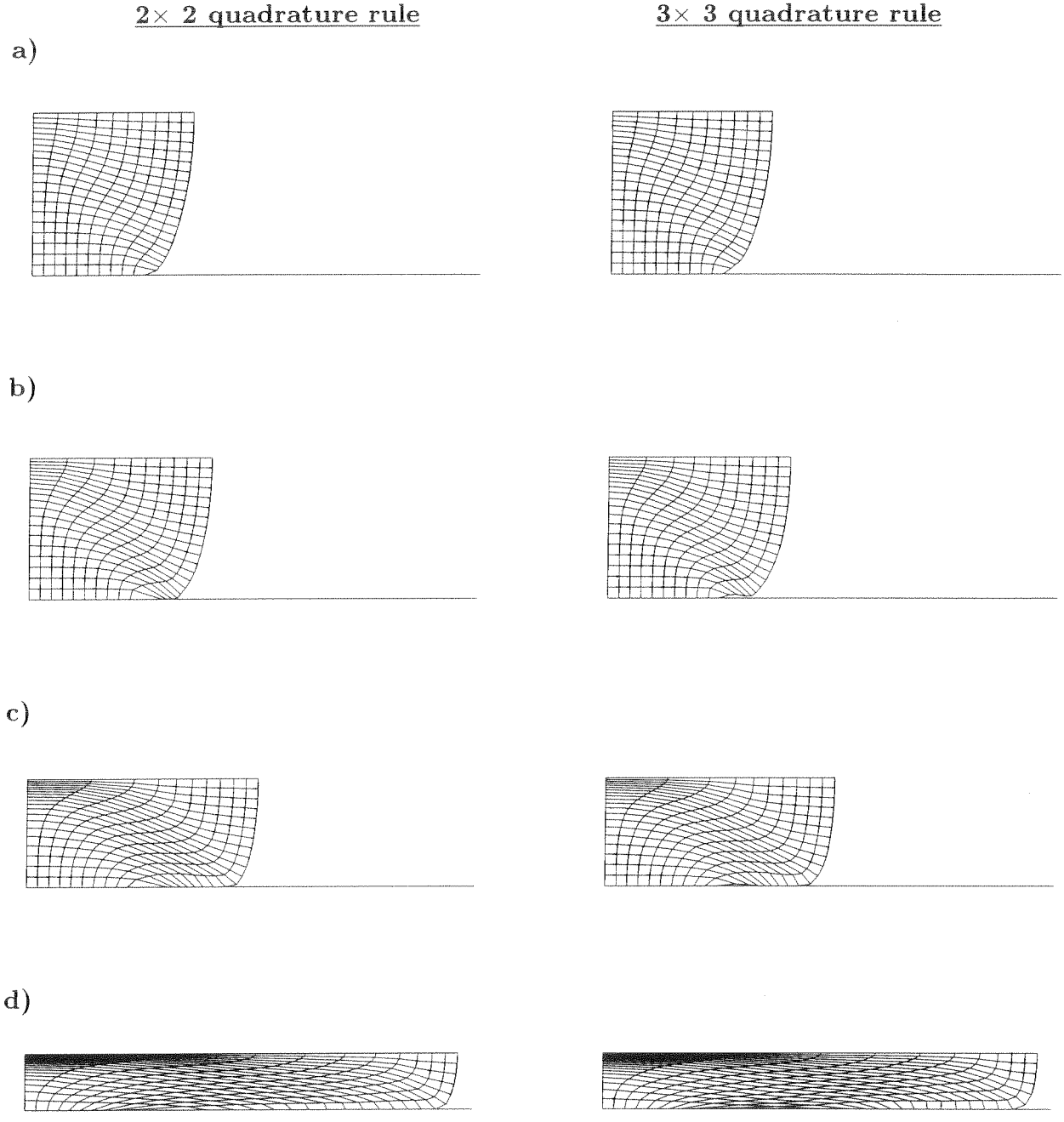

FIGURE 4.9. Deformed geometry of the elasto plastic block at a deformation stage of **a)** 25%, **b)** 35%, **c)** 50%, **d)** 74%, upsetting, for the Q1/ES4 element with the 2x2 point Gaussian integration rule (left column) and the Q1/ES4 element with the 3x3 point Gaussian quadrature rule (right column). The 5-point quadrature rules leads to results nearly identical to the 3×3 rule.

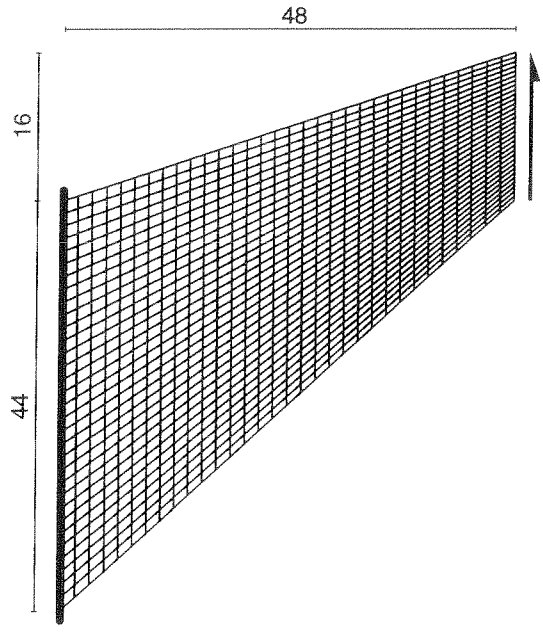

FIGURE 4.10. Cook's membrane problem. Initial configuration (32 × 32 element mesh).

3x3 point Gaussian integration rule, the element behaves rather stiffly. As observed in Figure 4.9, the element in the lower right corner resists to bend into a triangular shape, but a 90^o turn is finally accomplished at the end of the simulation. This stiff behavior is not so accused for the 2x2 point Gaussian integration rule. This difference response of the corner element leads to different sliding behavior at the contact interface, as observed in Figure 4.8. Using the element Q1/ES7 with three additional enhancement degrees of freedom this stiff response is diminished. It is to be note again that no hourglass modes appears in the simulation, leading to a smooth pattern of the deformation along all the loading process.

4.3. Cook's membrane problem

We next consider the benchmark test for bending dominated problems in plane strain referred to as the Cook's membrane problem. Figure 4.10 depicts the initial configuration of the problem. The problem consists of a tapered panel clamped on one end and subjected to a shearing load on the opposite end. As in SIMO & ARMERO [1992], two material models are considered. First, the Neo-Hookean model defined by the stored energy function (4.2), in regularized form, with material parameters $\Lambda = 40.0942 \cdot 10^4\ GPa$ and $\mu = 80.1938\ GPa$, leading to a quasi-incompressible response. Second, a J_2-finite strain plastic model as in

a)

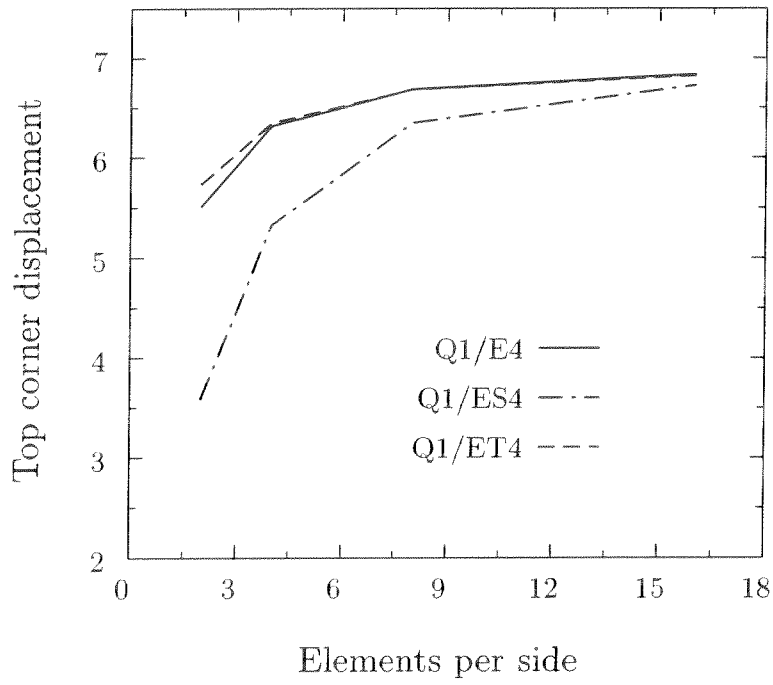

b)

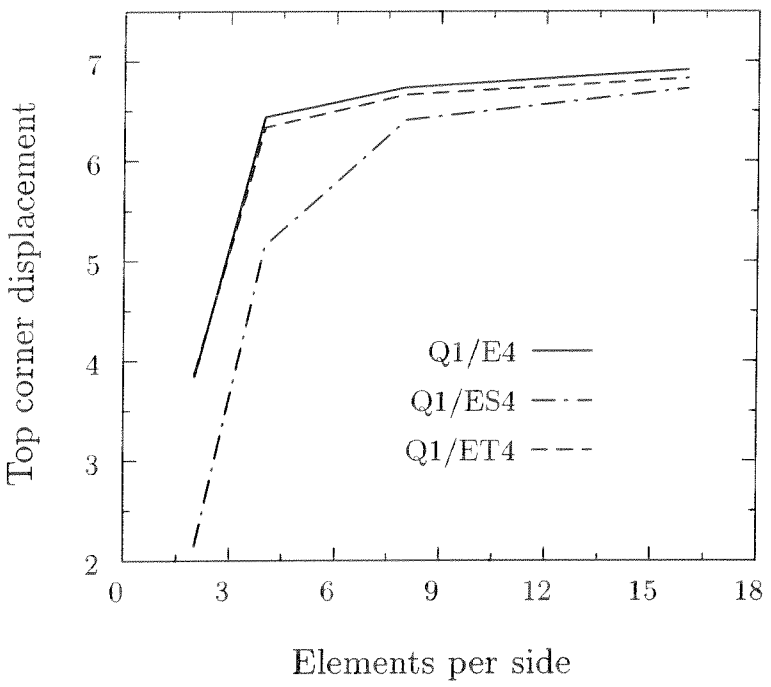

FIGURE 4.11. Cook's membrane problem. Convergence of finite element solutions: **a)** quasi-incompressible finite elasticity; **b)** finite strain J_2-flow theory.

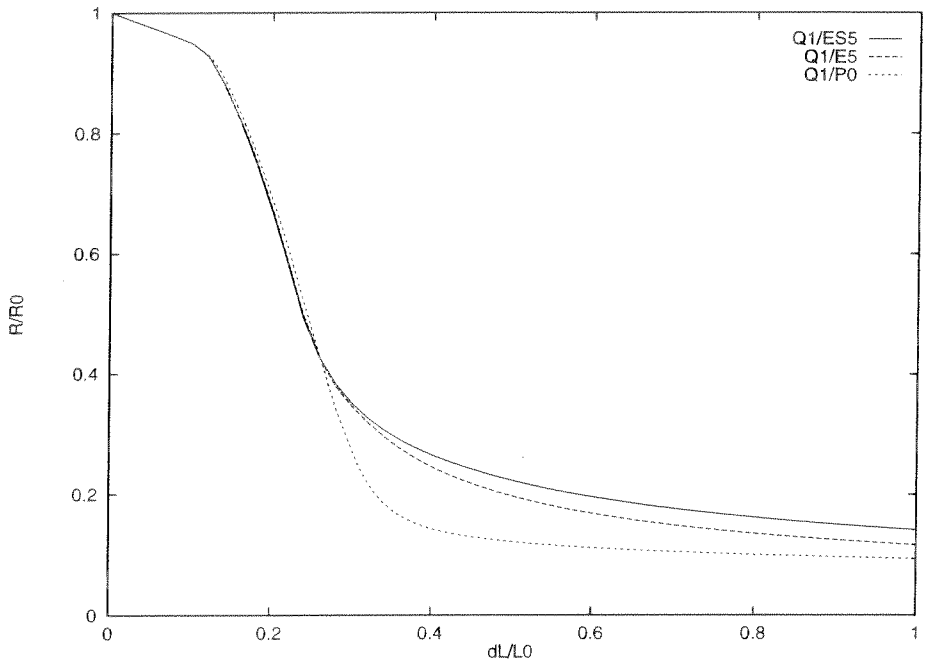

FIGURE 4.12. Axisymmetric necking of a circular bar. Relative ratio of the current radius at the center versus relative elongation.

SIMO & ARMERO [1992] in regularized form is considered. See this last reference for details, and Table 4.2 for the value of the assumed material parameters.

Figure 4.11 summarizes the convergence of the finite element solutions computed wit the Q1/E4, Q1/ES4 and Q1/ET4 elements. The vertical tip displacement (upper left corner) obtained for a applied load of 100 in the elastic case, and of 5 in the elastoplastic case, is plotted versus the number of elements per side. From these results, we observe that the Q1/ES4 results in a stiffer response in bending dominated problems for coarse meshes. This drawback is not shared by the Q1/ET4 quad, which leads to a good accuracy in these conditions.

4.4. Necking of a circular bar

The tension test of a circular bar has become a standard benchmark problem for finite element formulations at finite strain. A cylindrical bar with a radius of 6.413 *mm* and a length of 53.334 *mm* is considered. The necking is triggered with a small geometric imperfection, 1% reduction of the radius at the center of the bar. The J_2-flow theory finite strain elasto-plastic model described in SIMO & ARMERO [1992] is considered, with material properties summarized in Table 4.2. The bar is loaded in tension with a prescribed displacement at the top end.

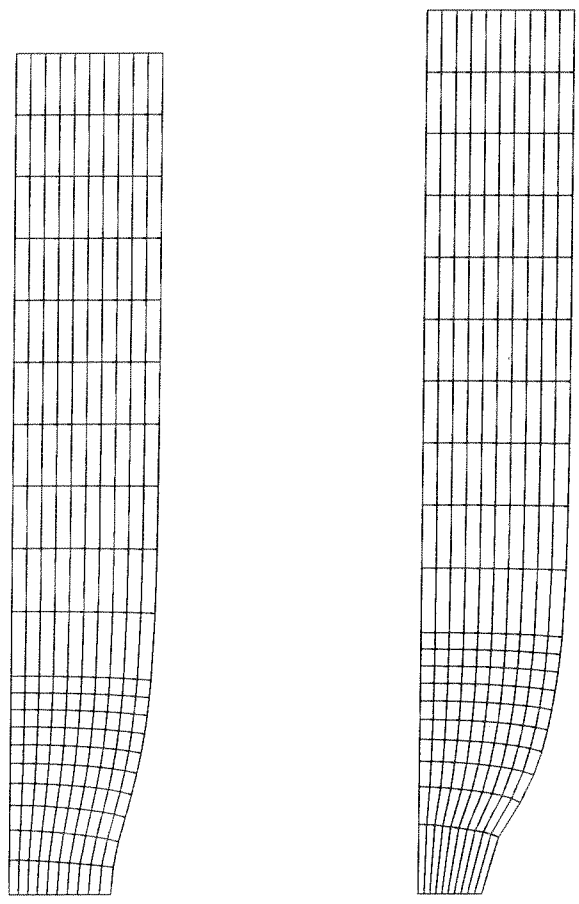

FIGURE 4.13. Axisymmetric necking of a bar. Deformed geometry obtained with the Q1/ES5 element at **a)** 5.6 top displacement, and **b)** 7.0 top displacement.

i. *Axisymmetric analysis.* The upper right quarter of the cross section of the bar is discretized using appropriate symmetry boundary conditions along the center line of the bar. The mesh consists of 200 axisymmetric Q1/ES5 elements. Simulations with the original Q1/E5 element have been reported in SIMO & ARMERO [1992].

Figure 4.12 depicts the computed radius at the center versus the total relative elongation of the bar. Nominal values with respect to the initial radius and length are reported. The curves obtained with the axisymmetric Q1/ES5 and the Q1/E5 elements are included. The 5-point integration rule is considered in both cases. For comparison, the curve for the Q1/P0 element is included in the figure. The deformed geometry of the cross section is shown in Figure 4.13 for a top displacement of 5.6 and 7.0. No hourglass modes are observed in any of the simulations.

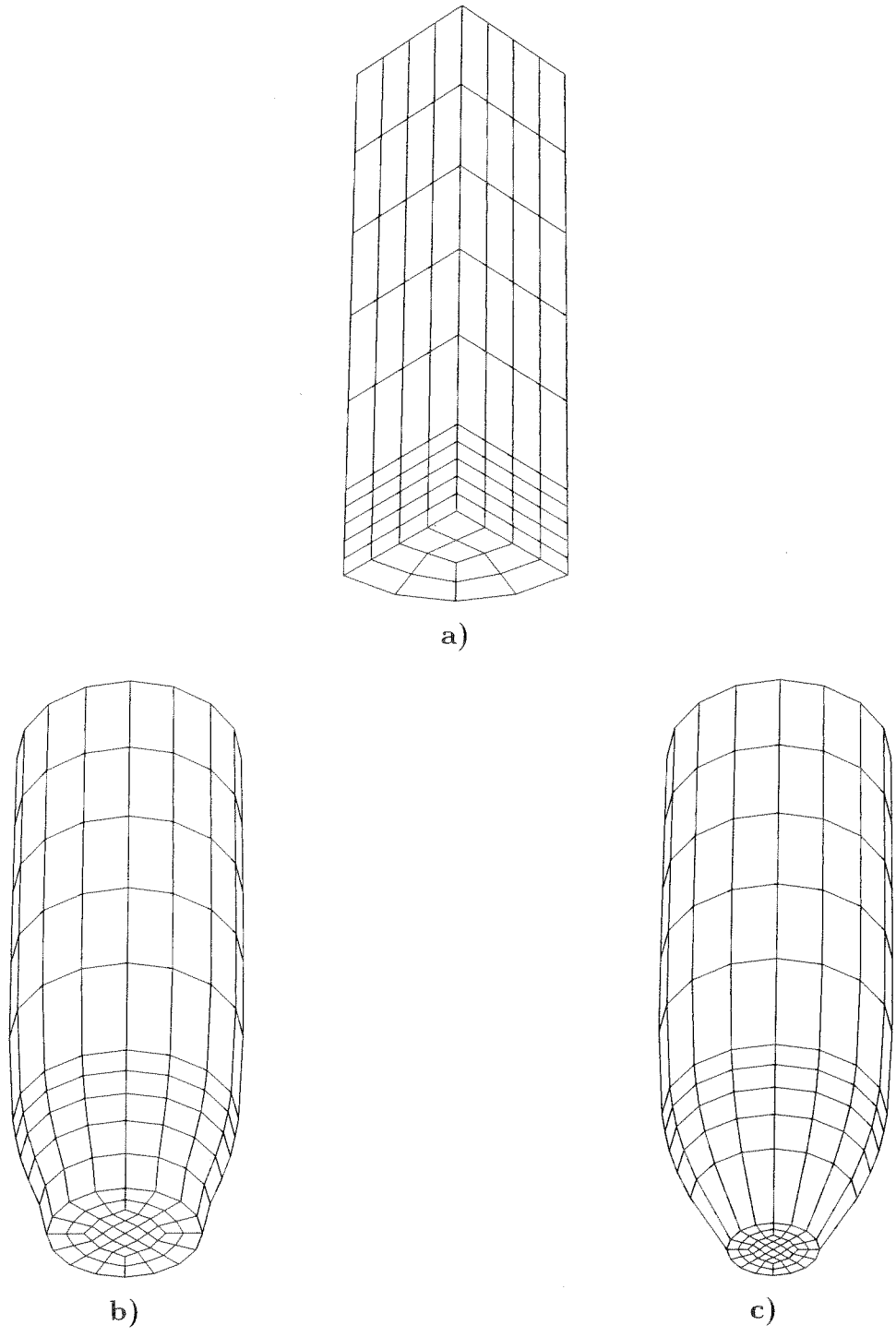

FIGURE 4.14. 3D necking of a bar. Solution obtained with the Q1/ES12 element **a)** Initial configuration, **b)** Solution at a top displacement of 5.6 mm, and **c)** Solution at a top displacement of 7.0 mm.

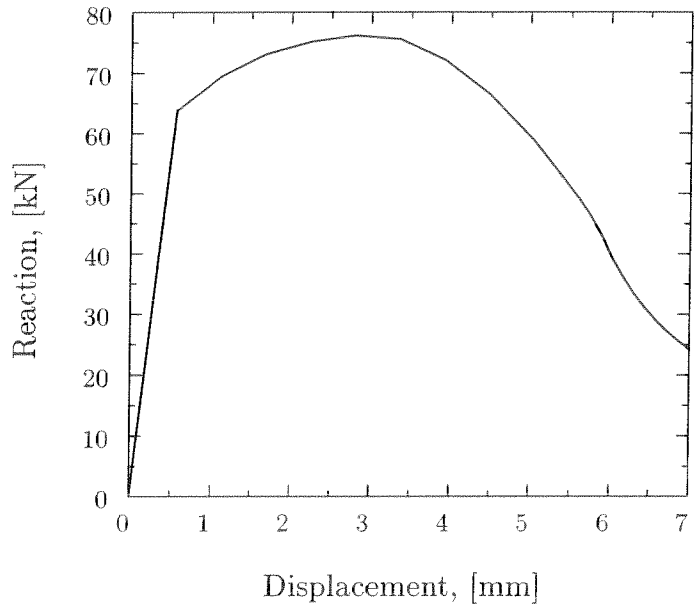

FIGURE 4.15. 3D necking of a bar. Load-displacement curve obtained with the Q1/ES12.

ii. *Three dimensional analysis.* A three dimensional simulation is carried out with the Q1/ES12 element described in Section 2.1. The initial configuration is depicted in Figure 4.14.a. An eight of the bar is discretized with a total of 120 elements. Appropriate symmetry boundary conditions are imposed on the lateral and bottom faces. Prescribed displacements are imposed at the top base. A $2 \times 2 \times 2$ Gaussian quadrature rule is employed. Figure 4.14 shows the solution obtained in this case at 5.6 *mm* and 7.0 *mm* imposed top displacement. The load-deflection curve is shown in Figure 4.15. No modes are observe in this test either.

4.5. Plane strain tension test

This example consists of the necking of a bar in plane strain. The specimen is 12.826 *mm* wide and a 53.334 *mm* long. The upper right quarter of the bar is discretized using appropriate symmetry boundary conditions along the center lines. The mesh consists of 200 plane strain Q1/ES4 elements. The elasto plastic material properties are summerized in Table 4.2. Figure 4.16 depicts the deformed configuration at a top displacement of 5.6 and 7.0.

An hourglass mode is observed in this case at large tensile strains, as shown in Figure 4.17. The appearance of this mode can be traced back to the presence to a limit point in the load/displacement law in tension, thus leading to a negative stiffness for the stretching mode. This negative stiffness is communicated to the two bending modes shortly after the limit point of the graph is reached. While the negative stiffness of the tension mode is

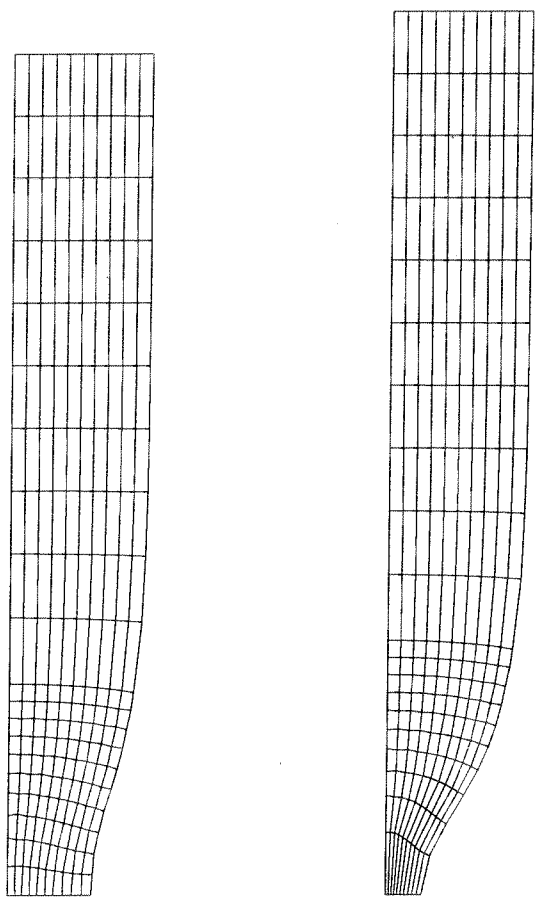

FIGURE 4.16. Plane strain tension test. Deformed geometry at **a)** 5.6 top displacement, and **b)** 7.0 top displacement.

physical in nature, the negative stiffness of the bending modes is numerical, and directly related to the design of the response of the element in bending. Unfortunately the bending modes follow the behavior of the tension mode becoming softer under tension. These modes are able to propagate through the mesh showing typical hourglass patterns. Using 2x2 point Gaussian integration, the situation is worse than employing 3x3 point Gaussian integration or 5-point integration rule. The hourglassing can be avoided by adding a control term of the form

$$\int_V \alpha \left(\det(\mathbf{1} + \tilde{\boldsymbol{F}}) - 1\right)^2 \mathrm{d}V \tag{4.5}$$

to the functional (3.5), which gives additional stiffness to the volumetric part of the enhanced deformation gradient. A small factor of $\alpha = 1.$ is sufficient to stabilize the hourglassing as can be seen in Figure 4.17.b. A similar strategy has been proposed in WRIGGERS

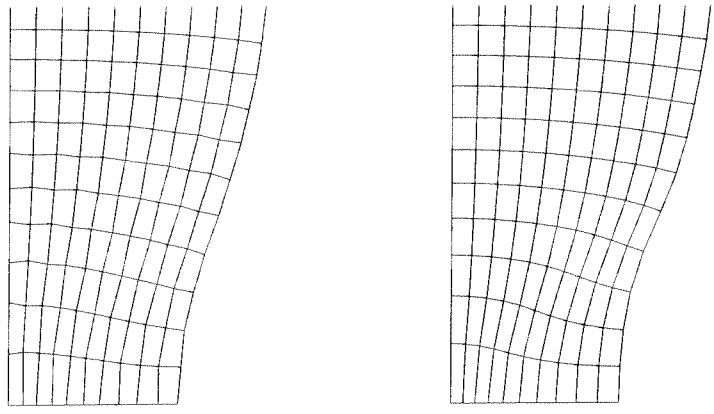

a) b)

FIGURE 4.17. Plane strain tension test. **a)** Hourglass modes in the necking zone at 5.6 top displacement. **b)** Necking zone at 5.6 top displacement obtained by Q1/ES4 element with hourglass stabilization.

& REESE [1995] to alleviate the hourglass modes of the original enhanced formulation in compression. Alternative strategies to avoid this mode are currently under further investigation.

5. Concluding Remarks

Very simple modifications of existing enhanced finite elements have been proposed that leads to a significant improvement in the numerical performance. The first modification involves a symmetric enhancement, and it is very easily incorporated in current implementations of the original formulation. It has been observed that the transpose part of the original enhancement is enough to eliminate the zero energy energy modes, thus leading to a second family of elements. No hourglass modes have been observed in compression for these new formulations.

As it happens with the original and the different enhanced strategies tested to date, the element shows hourglass modes at high tensile strains for some inelastic models. These modes appear in severely strained materials exhibiting a negative stiffness in tension (i.e., after passing a limit point). This negative stiffness, although physical, is communicated to the bending modes of the element, leading to an hourglassing pattern. Hourglass control is shown to suppress these modes. Alternative strategies for the elimination of this undesirable response are currently under further investigation.

Acknowledgments: We are indebted to Professor Robert L. Taylor for many helpful discussions and for making available his finite element code FEAP. Part of the numerical

simulations presented above where obtained after implementing the elements proposed herein in this code.

References

CRISFIELD, M.A.; G.F. MOITA; G. JELENIC; L.P.R. LYONS and D.R.J. OWEN [1995] 'Enhanced lower-order element formulation for large strains' *Computational Plasticity IV – Fundamentals and Applications – Proceedings of the 4th international conference*, ed. by D.R.J. Owen, E. Onate.

NAGTEGAAL; J.C. and D.D. FOX [1995] "using assumed enhanced strain elements for large compressive deformation," *Int. J. Solid Struct.*, to appear.

SIMO, J.C. and S. RIFAI [1990] "A class of mixed assumed strain methods and the method of incompatible modes" *Int. J. Numer. Methods Eng.*, **29**, 1595-1638.

SIMO J.C. and F. ARMERO [1992] "Geometrically non-linear enhanced strain mixed methods and the method of incompatible modes," *Int. J. Numer. Methods Eng.*, **33**, 1413-1449.

SIMO, J.C.; F. ARMERO and R.L. TAYLOR [1993] "Improved versions of assumed enhanced strain tri-linear elements for 3D finite deformation problems," *Comp. Meth. Appl. Mech. Eng.*, **110**, 359-386.

SOUZA NETO, E.A.; D. PERIC, G.C. HUANG and D.R.J. OWEN [1995] "Remarks on the stability of enhanced strain elements in finite elasticity and elastoplasticity," *Computational Plasticity IV – Fundamentals and Applications – Proceedings of the 4th international conference*, ed. by D.R.J. Owen, E. Onate.

TAYLOR, R.L.; P.J. BERESFORD and E.L. WILSON [1976] "A non-conforming element for stress analysis," *Int. J. Numer. Methods Eng.*, **10**, 1211-1219.

WRIGGERS, P. and S. REESE "A note on enhanced strain methods for large deformations," *Comp. Meth. Appl. Mech. Eng.*, to appear.